Icarus 223 (2013) 444–459

Contents lists available at SciVerse ScienceDirect

Icarus

journal homepage: www.elsevier.com/locate/icarus

The Meteoroid Input Function and predictions of mid-latitude meteor observations by the MU radar

Steven Pifko [a,*], Diego Janches [b], Sigrid Close [a], Jonathan Sparks [c], Takuji Nakamura [d], David Nesvorny [e]

[a] Space Environment and Satellite Systems Lab, Department of Aeronautics and Astronautics, Stanford University, Palo Alto, CA 94305, USA
[b] Space Weather Lab, Goddard Space Flight Center, NASA, Greenbelt, MD 20771, USA
[c] Department of Physics, University of Washington, Seattle, WA 98105, USA
[d] National Institute for Polar Research, Tokyo, Japan
[e] South West Research Institute, Boulder, CO 80302, USA

ARTICLE INFO

Article history:
Received 11 June 2012
Revised 13 October 2012
Accepted 15 December 2012
Available online 12 January 2013

Keywords:
Meteors
Radar observations
Instrumentation

ABSTRACT

The majority of extraterrestrial particles entering Earth's atmosphere originate from the Sporadic Meteoroid Complex (SMC) and are associated with many mesospheric layer phenomena. The Meteoroid Input Function (MIF) is a model that has been developed with the purpose of understanding the temporal and spatial variability of the meteoroid impact in the atmosphere. The MIF has been shown to accurately predict the seasonal and diurnal variations of the meteor flux observed by High Power Large Aperture (HPLA) radars at various geographic locations, including the Arecibo Observatory (AO) and the Poker Flat Incoherent Scatter Radar (PFISR). For this, the model requires the assessment of a potential observational bias of the particular HPLA radar utilized: the minimum detectable radar cross-section (RCS). The RCS sensitivity threshold provides a metric to characterize the radar system's ability to detect particles with a given mass and speed. In this paper, the MIF model was used to predict meteor properties (e.g. the distributions of areal density, speed, and radiant location) observed by the Middle and Upper atmosphere (MU) radar while leveraging the system's interferometric capability to address the model's ability to predict meteor observations at middle geographic latitudes and for a radar operating frequency in the low VHF band. This study demonstrates that the MIF accurately considered the speed and sporadic source distributions for the portion of the meteoroid population observable by the MU radar, and the applicability of the MIF to the MU system increases the confidence of using it as a global model.

1. Introduction

The majority of extraterrestrial particles entering Earth's atmosphere originate from the Sporadic Meteoroid Complex (SMC) and are in the mass range of 10^{-11}–10^{-4} g (Ceplecha et al., 1998; Baggaley, 2002; Williams and Murad, 2002). These sub-millimeter sized meteoroids enter the atmosphere at speeds between 11 and 72 km/s (Close et al., 2002) and subsequently collide with air molecules, causing heating and ablation of the incoming particles, which releases both neutral and ionized atoms from the meteoroid as well as ionizes the surrounding atmosphere. As a result, meteoroids deposit large amounts of metallic atoms (e.g. Si, Na, Fe, K, and Ca) in the Mesosphere and Lower Thermosphere (MLT), mostly over the altitude range of 70–140 km (Janches et al., 2003, 2009; Vondrak et al., 2008), and provide the dominant source of metals associated with many mesospheric layer phenomena (Plane, 2003). Moreover, similar ionized layers have been observed in other planetary atmospheres (e.g. at an altitude of approximately 90 km on Mars, 120 km on Venus, and 550 km on Titan; Kliore et al., 2008; Patzold et al., 2005, 2009; Withers et al., 2008).

The Meteoroid Input Function (MIF) is a model developed to provide a global view of the diurnal and seasonal variations of the incoming meteoroid flux with the purpose of better understanding its relation to atmospheric phenomena in the MLT (Janches et al., 2006; Fentzke and Janches, 2008; Fentzke et al., 2009). The MIF assumes that the sporadic meteoroid population is distributed among the six known apparent sources: the North and South Apex, the Helion and Anti-Helion, and the North and South Toroidal (Jones and Brown, 1993; Taylor, 1997; Taylor and Elford, 1998). Assuming a global meteoroid mass input into the atmosphere (Ceplecha et al., 1998), the orbits of individual meteoroids were simulated by using Monte Carlo techniques to assign an initial speed and radiant to each modeled particle from the observed distributions of the SMC apparent sources. As a result, the MIF predicts the overall meteoroid input to the MLT at any location on the Earth at any time of year and time of day.

The validation of the MIF model requires comparison with observations of the meteoroid atmospheric input. There are

* Corresponding author.
E-mail address: spifko@stanford.edu (S. Pifko).

0019-1035/$ - see front matter © 2013 Elsevier Inc. All rights reserved.
http://dx.doi.org/10.1016/j.icarus.2012.12.014

various types of ionization regions associated with the meteoroid's atmospheric entry process, which are collectively referred to as the meteor (Janches et al., 2003). In particular, there is a relatively small plasma region surrounding and moving with the meteoroid, known as the meteor head (Janches et al., 2000; Close et al., 2002). High Power Large Aperture (HPLA) radar systems efficiently detect this target and have been extensively used over the past decade for various investigations that address issues related to plasma physics, space and Solar System sciences, and astronomy (Janches et al., 2008). These instruments are capable of determining the meteoroid's range and range rate with high precision, and in some cases, the object's position and velocity vectors may be calculated, thus allowing for the estimation of orbital properties (Chau and Woodman, 2004; Sparks et al., 2010; Kero et al., 2011). HPLA systems are also effective at detecting the evolution of these quantities along the meteor path, and thus, they enable the study of various physical processes regarding the meteoroid mass loss mechanisms through either the dynamic or scattering behavior of the meteor (Close et al., 2004; Janches et al., 2009).

In order to accurately compare the model simulations with observations, the MIF produces expected meteor detection rates of specific HPLA radar systems for a given time and location. For this, considerations on sensitivity limitations of the particular HPLA instrument are utilized in order to characterize the portion of the incoming meteoroid population that is detectable by the specific radar (Close et al., 2005; Janches et al., 2008). An example of the large difference in distribution of meteor detections that can arise from using different observing instruments was shown by the meteor studies conducted with the 430 MHz Arecibo Observatory (AO) radar in Puerto Rico (~18°N) and the 440 MHz Poker Flat Incoherent Scatter Radar (PFISR) in Alaska (~67°N), in which both systems operated at a similar transmitting power and frequency yet had different aperture (Fentzke et al., 2009). The difference in radar aperture yielded a considerable difference in detection sensitivity, and thus, there was a significant difference in the spectrum of meteoroid mass and velocity that each radar system was capable of observing. In addition, there is an extreme difference in geographic latitude between the two radar locations, which caused a difference in the portion of the SMC that each radar system observed. Nonetheless, the meteor detection rate of both HPLA systems and the seasonal and geographical variability of the incoming meteoroid flux were successfully captured by the MIF (Fentzke et al., 2009).

The nature of the MIF and its development suggest that further comparison to meteor observations conducted by additional radar systems is necessary in order to better assess the accuracy of the model and to improve it as needed. In particular, utilizing systems with different transmitting power and frequency improves the confidence in the modeling of the physical considerations that determine radar sensitivity. For that purpose, this paper presents the simulation of meteor observations obtained with the 46.5 MHz Middle and Upper atmosphere (MU) radar in Japan, offering the opportunity to validate the temporal variations modeled with the MIF at middle geographic latitude as well as the radar sensitivity considerations at the VHF frequency range. Lastly, the results presented here have the novel aspect that the MU radar system possesses the ability to obtain directional information from the detected meteors through the simultaneous use of several receiving channels, thus enabling the determination of the meteor radiant locations for the particle detections. This allows for the validation of the assumptions made regarding the sporadic meteor source and speed distributions used as inputs to the MIF.

A description of the MIF model is presented in Section 2 along with the model's application used to simulate the meteoroid input at the geographic location of the MU radar. The meteor experiment conducted at MU and the characterization of the meteor detection sensitivity of the MU radar system are addressed in Section 3. Section 4 presents the results of the experiment by providing a comparison between the observed data and the model predictions. Lastly, the conclusions and final remarks are discussed in Section 5.

2. The Meteoroid Input Function (MIF): model description and application

The MIF is an empirical model developed for the purpose of providing a global description of the diurnal, seasonal, and geographical variability of the meteoroid input in the upper atmosphere. This knowledge is required to better assess the relationship between the incoming flux and the chemistry and composition of the MLT (Janches et al., 2006; Gardner et al., 2011). The model, described in detail by Fentzke and Janches (2008), incorporates a global mass flux input into Earth's atmosphere (Ceplecha et al., 1998) that was divided among the apparent sporadic meteoroid sources (Jones and Brown, 1993), each of which was represented as a Gaussian distribution of meteoroid speed and radiant, to give a statistical distribution of the SMC in the MLT by using Monte Carlo techniques to simulate millions of meteoroid orbits. The North and South Apex sources were modeled collectively as approximately 33% of the meteoroids at 1 AU. The remaining two-thirds of incoming meteoroids was divided among the other apparent sources, with the Helion and Anti-Helion sources each contributing nearly 22%, and the North and South Toroidal each providing 11% of the total flux. The speed distribution for each source was based on radar observations from various studies, using both HPLA and meteor radar systems. The Apex source was modeled as bimodal with approximately 80% of the particle speeds centered at 55 km/s and 20% centered at about 17 km/s (Janches et al., 2003; Sulzer, 2004; Janches and Chau, 2005). The remaining radiant sources (i.e., the Helion, Anti-Helion, and North and South Toroidal) were modeled as Gaussian with a peak at 30 km/s (Jones and Brown, 1993). Each of the apparent sources was modeled with the same particle mass distribution derived from the incoming mass–flux curve published by Ceplecha et al. (1998), which combined the results of several studies to estimate a global influx over the mass range of 10^{-18}–10^{18} g and showed that the number of incoming meteoroids increases approximately exponentially with decreasing mass. The MIF models particles within the range of 10^{-11}–10^{-4} g; however, for the purpose of this work the results presented only include particles in the mass range of 10^{-7}–10^{-4} g. Particles in this range ablate and produce electrons independent of speed (Bronshten, 1983; Vondrak et al., 2008), but the ability to detect them is strongly dependent on the radar system utilized (see Section 3.2). Tables 1 and 2 summarize the modeled distributions, organized by sporadic source, of the meteoroids that were visible over the geographic latitude of the MU radar. The columns in Table 1 present the mean and standard deviation of the speed, ecliptic longitude (λ), and ecliptic latitude (β) distributions for the sources. The ecliptic longitude is the angle of rotation about the ecliptic normal measured from the Earth–Sun direction, and the ecliptic latitude is the angle of rotation out of the ecliptic plane (i.e., the Sun is located at $\lambda = 0°$, $\beta = 0°$). Meanwhile, Table 2

Table 1
MIF modeled distributions of speed, ecliptic longitude, and ecliptic latitude for the meteoroids that were present above the geographic location of MU.

Source	Speed (km/s)	λ (°)	β (°)	σ_{Spd} (km/s)	σ_λ (°)	σ_β (°)
Apex (fast, slow)	55, 19	270	12	6.6, 5.0	19	30
Helion	30	349	2	6.6	16	16
Anti-Helion	30	189	3	6.6	18	18
North Toroidal	30	270	58	6.6	19	20
South Toroidal	30	270	–	6.6	16	–

Table 2
MIF modeled contributions of each sporadic source to the meteoroid population above the geographic location of MU.

Source	Relative contribution (%)				
	Average	Spring	Summer	Autumn	Winter
Apex (fast, slow)	29.8 (97, 3)	27.4 (97, 3)	29.3 (97, 3)	32.9 (97, 3)	29.0 (97, 3)
Helion	23.0	25.0	28.0	21.6	17.8
Anti-Helion	23.1	26.3	19.0	19.5	28.5
North Toroidal	20.0	20.0	19.6	19.8	20.5
South Toroidal	4.1	1.2	4.2	6.2	4.2

provides the relative strength of contribution of each source, given as yearly and seasonal averages.

Each simulated particle of the MIF was given an initial radiant location, which was based on the statistical distribution of the apparent sporadic meteoroid sources. This initial condition was used in this study to assign the sporadic source from which the meteoroid originates and was determined by the proximity to the center locations of the six sporadic meteoroid apparent sources. The North and South Apex sources lie just above and below the direction of Earth's velocity vector, with center points (λ, β) at (270°, 20°) and (270°, −20°), respectively. Likewise, the North and South Toroidal sources are above and below the Apex sources and are centered at (270°, 60°) and (270°, −60°), respectively. The Helion direction is towards the Sun (0°, 0°), and the Anti-Helion is in the opposite direction (180°, 0°). In the MIF simulations, the apparent source center that is closest to the particle radiant was considered to be the source of the particle and was the basis for determining the statistical distributions associated with each source presented in Tables 1 and 2.

2.1. Diurnal rates of meteoroid areal density

The predicted rate of meteoroid counts per unit area, referred to here as the meteoroid areal density, at the MU radar latitude during the specified observation times is shown in Fig. 1. It is important to note that the rates presented in the figure do not represent detectable events but instead incoming particles in the mass range 10^{-7}–10^{-4} g that formed meteors at the specified geographic location (i.e., a meteor is formed but the MU radar may not have detected it), assuming that the total meteoroid mass input was that given by the MIF and reported by Ceplecha et al. (1998). From the panels in the figure, it is evident that there was a seasonal variability of the meteoroid areal density in both the total number and shape distribution of the diurnal rate. As expected, the peak of the daily meteoroid flux occurred during the autumnal equinox since this was when the Apex sources reached their highest elevation in the Northern Hemisphere sky. Conversely, the daily minimum occurred during the spring equinox when the highest elevation that the Apex sources reached during the day was lowest, with a large portion of the South Apex never reaching an elevation higher than the local horizon (Fentzke and Janches, 2008). In addition, when comparing the observation times of the winter and summer solstices, it was seen that for the December period there was a sharper increase in the number of meteoroids in the early morning, while during the June period there was a steeper decrease in meteoroid activity in the late morning and early afternoon. This was caused by the changing orientation of the Helion and Anti-Helion sporadic sources during the year with respect to the MU radar location, which was significant in determining the amount of activity around local midnight and noon. In December, the Anti-Helion radiant reached higher elevation than the Helion in the Northern Hemisphere sky; whereas in June, the situation reversed, introducing seasonal variability around the midnight and noon periods (Janches et al., 2006). In general however, at mid-northern latitude the simulated seasonal effects on the meteoroid input were not as pronounced as they were at higher latitudes (Janches et al., 2006; Fentzke et al., 2009; Sparks et al., 2009). The peak rate for meteoroids in the 10^{-7}–10^{-4} g mass range at the seasonal maximum (i.e., autumn) was estimated to be approximately 16 meteoroids/km^2/min, compared to about 11 meteoroids/km^2/min during the minimum activity period (i.e., spring).

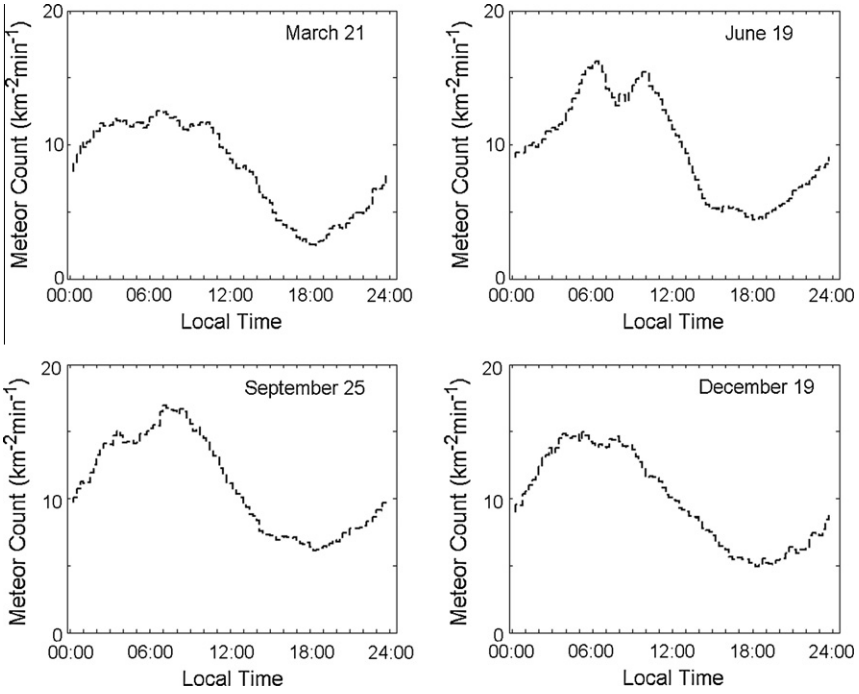

Fig. 1. MIF modeled diurnal rate of meteoroid areal density at the MU radar geographical location during the observation times for the meteoroid mass range 10^{-7}–10^{-4} g.

Finally, it is clear from Fig. 1 that for each day there was a predicted peak in meteoroid activity at 06:00, local time, when the Apex reached its highest point in the sky relative to the observer (i.e., the MU radar). The minimum in meteoroid areal density occurred at 18:00 for all observing periods as most of the sporadic sources were below the local horizon at this time of day. Since the meteor observations conducted with MU were taken over the four different simulated 24-h periods, it is expected that the features evident in the modeled diurnal variation of meteor activity will be prominent in the observed data. This analysis is presented in Section 4.2.

2.2. Distributions of meteoroid speed and radiant

In addition to the rate of meteoroid areal density, the simulated speed and radiant distributions for the incoming meteoroids are presented in Figs. 2 and 3, respectively. From these figures it can be derived that, as expected, the majority of the modeled meteoroid input in the 10^{-7}–10^{-4} g mass range was provided by slower particles originating from the non-Apex sporadic sources. This is evident from the dominant peak in Fig. 2 at approximately 30 km/s, as opposed to the secondary peak at 55 km/s, indicating that the majority of particles had the expected speed of the non-Apex meteoroids.

The radiant maps given in Fig. 3 show the modeled meteoroid radiant in terms of ecliptic longitude (λ) and latitude (β) and represent the point in the sky that the meteoroids entered into a hyperbolic geocentric orbit (Jones and Brown, 1993). The radiant angles are defined as in Section 2, where the ecliptic longitude is the angle of rotation about the ecliptic normal measured from the Earth–Sun direction, and the ecliptic latitude is the angle of rotation out of the ecliptic plane (i.e., the Sun is located at $\lambda = 0°$, $\beta = 0°$). The plots in Fig. 3 are oriented such that the center point corresponds to the Apex direction (i.e., the direction of Earth's velocity relative to the Sun, $\lambda = 270°$, $\beta = 0°$). The locations of the six sporadic meteoroid sources are also displayed in the figure as ellipses, with the coordinates as specified in Section 2. The North and South Apex sources lie just above and below the figure center point, respectively. Likewise, the North and South Toroidal sources are above and below the respective Apex sources. To the left of the Apex is the Helion direction, and the Anti-Helion is symmetrically opposite the Helion source about the Apex. Note that contributions from all of the sporadic sources were considered in the MIF and are clearly visible in Fig. 3.

It is important to note, once again, that the distributions presented in Figs. 2 and 3, also summarized in Tables 1 and 2, are the results from the MIF previous to taking any consideration of the detection capability of the MU radar system.

It is also evident from the radiant maps in Fig. 3 that, given a constant global meteoroid input, the relative contributions of the South Apex, Helion, Anti-Helion, and South Toroidal sources to the local MLT showed a seasonal variability. For example, the Helion and Anti-Helion sources provided a similar contribution of meteoroids to the MLT at mid-northern latitude in March and September. However, during December and June, one source contributed more meteoroids than the other. This is consistent with the relative steepness in the increase and decrease of expected meteoroid activity in the observation dates for each season, as shown in Fig. 1 and discussed in Section 2.1. Additionally, the radiant distributions in Fig. 3 highlight the overall meteoroid activity for each observation period. In September, when meteor activity was at its peak in the Northern Hemisphere, there were clear contributions from each of the sporadic meteor sources, and there was a very strong contribution from the North Apex. On the remaining dates, it can be seen that some portions of the radiant map were cut off from appearing over MU, and the relative strength of the

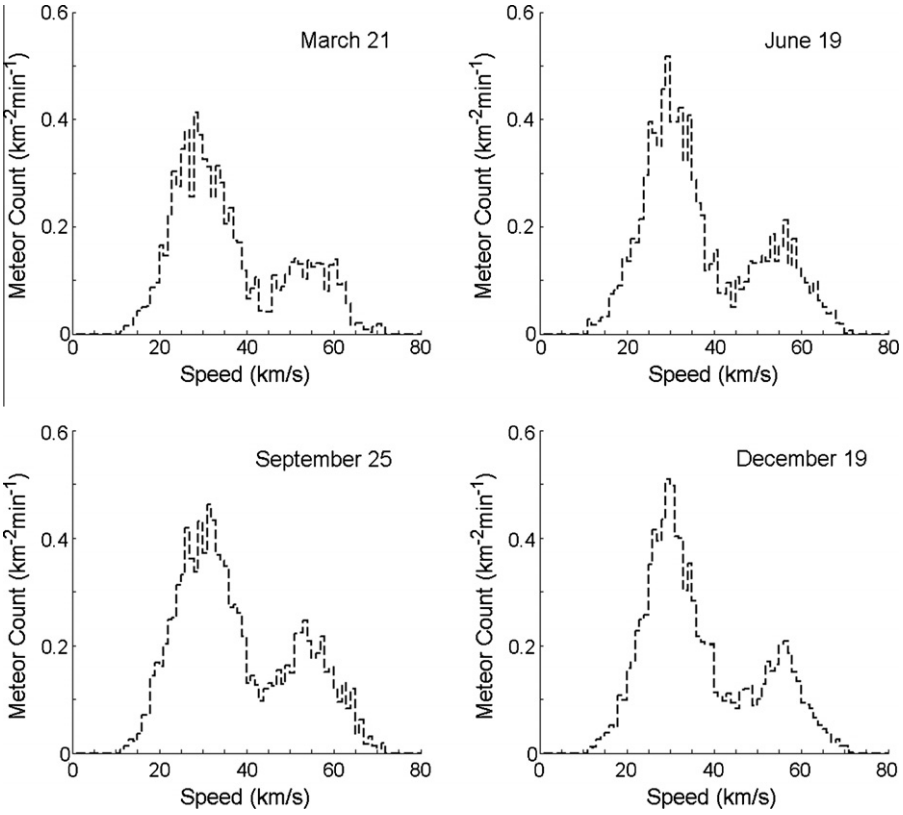

Fig. 2. Expected incoming speed distribution over the MU radar location for each of the experiment dates and meteoroid mass range 10^{-7}–10^{-4} g, as modeled by the MIF.

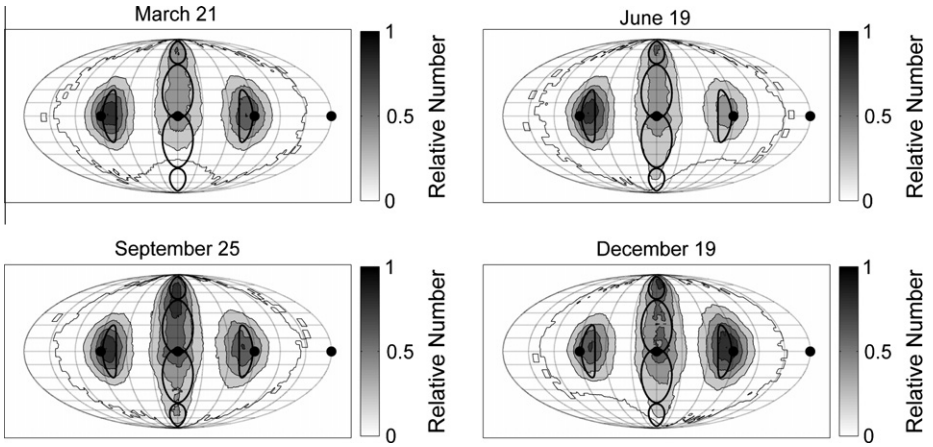

Fig. 3. Expected radiant distribution observable from the MU radar location for each of the experiment dates and meteoroid mass range 10^{-7}–10^{-4} g, as modeled by the MIF.

Apex sources was less than it was during September. The observation period in March demonstrated the inability to observe meteors with high southern ecliptic latitude radiant locations, and logically, this coincided with the time of year when meteoroid activity was at a minimum in the Northern Hemisphere. During this period, there was no contribution from the South Toroidal source and a reduced contribution from the South Apex source at mid-northern latitude. As in the case with the modeled variability of the diurnal rate of meteoroid areal density, these features are expected to be consistent with the MU observations, and the predicted and observed radiant maps are compared in Section 4.4 to further validate the assumptions made by the MIF and the estimated input parameters used in the model.

3. The MU radar

3.1. Meteor observations description

The MU radar is located in Shigaraki, Shiga Prefecture, Japan, at a geographic mid-latitude location (34.85°N, 136.10°E) and has been utilized for over a decade for various studies involving meteor observations (Sato et al., 2000; Fujiwara et al., 2007; Kero et al., 2011). The MU radar consists of 475 Cross-Yagi antennas arranged in a 103 m diameter circular array operating in the VHF band at 46.5 MHz and transmits a peak power of 1 MW.

For the purpose of this work, meteor observations using the MU radar were conducted over four distinct 24-h periods near the equinoxes and solstices (December 18–19, 2008, and March 20–21, June 18–19, September 24–25, 2009). These observation periods were specifically scheduled with the purpose of observing both the diurnal and seasonal variations in meteor activity at a mid-latitude geographic location. For the observations reported in this work, an uncoded radar pulse of 64 μs was transmitted with an interpulse period (IPP) of 1.28 ms and a sampling frequency of 2 μs (i.e., 300 m range resolution). This scheme allowed for the probing of the altitude range between 79.5 and 139.2 km. In addition, the MU radar possesses 25 receiving channels, which enabled simultaneous reception with independent sub-sections of the antenna array and thus allowed for highly sensitive interferometric measurements (Hassenpflug et al., 2008). For the case of meteor detections, this provided the capability to determine the meteoroid's vector position and velocity, which gave orbital information for each detected event. For the observations presented here, however, only four receiving channels were utilized, but nevertheless interferometric capability was still maintained (Nishimura et al., 2001). Fig. 4 shows an example of a meteor event observed during the March campaign and summarizes the identification and analysis technique utilized. Fig. 4a (upper left) shows the Range–Time–Intensity (RTI) plot from the signal recorded by one of the receiving channels (see Fig. 1 in Nishimura et al., 2001). The rectangular shape of the meteor head echo was due to the transmitted pulse shape (Sparks et al., 2009). Fig. 4b (upper right) shows the Signal-to-Noise Ratio (SNR) of the same event. The overall 'bell' shape on the SNR curve was produced by the meteor traveling through the radar beam. It is important to note that the short-lived SNR enhancement occurring at approximately 0.03 s after the meteor was first detected was likely produced by the fast ablation of the alkali metals present in the meteoroid body (Vondrak et al., 2008; Janches et al., 2009). By cross-correlating the received raw voltages among the different channels, the phase differences between the received signals were obtained, as seen in Fig. 4c (middle left). This information was then utilized to calculate the elevation and azimuth of each IPP during which the meteor was detected (Nishimura et al., 2001; Chau and Woodman, 2004; Sparks et al., 2010), displayed in Fig. 4d (middle right). The line-of-sight velocity, which in this case was the vertical velocity, may be obtained from measuring either the rate of change of the meteor head echo altitude or the Doppler shift in the received signal. The absolute direction of the meteor was obtained from the measured range, azimuth, and elevation, as shown in Fig. 4e and f (lower left and right, respectively). This provided a complete set of parameters to allow orbit determination.

The search and analysis of meteor events in the raw data followed the same methodology that has been applied to similar observations using the PFISR system (Sparks et al., 2010), where the only difference was in the manner in which the Doppler radial velocity was estimated. For the 440 MHz UHF operating frequency of PFISR, the Fast Fourier Transform (FFT) of the received signal in one IPP provided a sufficiently narrow spectrum to enable the accurate determination of the returned signal Doppler shift (Sparks et al., 2009). However, for the 46.5 MHz operating frequency of MU, the spectrum was as broad as the radar bandwidth. The Doppler signature was then calculated by applying a pulse-to-pulse correlation function between consecutive IPPs (Hagen and Farley, 1973; Mathews, 1976; Janches et al., 2000).

3.2. Radar characterization

When using instrumentation to conduct scientific experiments, it is necessary to characterize the biases and limitations introduced by the instruments being employed. For the case of meteor head echo observations with HPLA radars, it is inaccurate to generalize

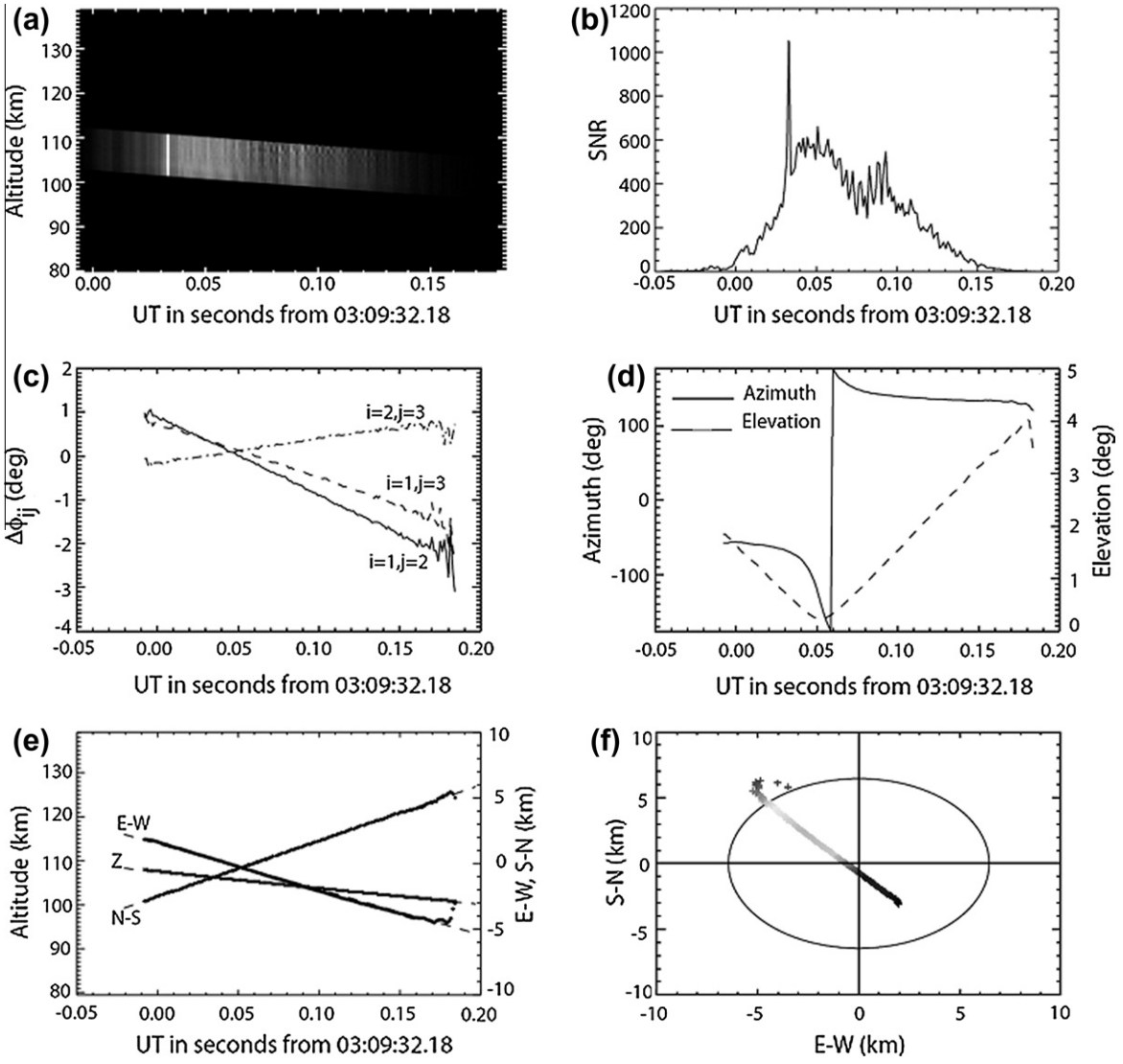

Fig. 4. Example meteor event detected by the MU radar system during the March observations: (a) Range–Time–Intensity (RTI) plot taken from one of the receiving channels; (b) Signal-to-Noise Ratio (SNR) of the event; (c) calculated phase difference between the received signals; (d) azimuth and elevation for each interpulse period in which the event was observed; (e) altitude of the detected meteor; (f) horizontal position of the detected meteor.

these system limitations over the entire radar class. Instead, each HPLA radar must be characterized and considered individually since the instruments are very different in comparison to each other (Janches et al., 2008), and furthermore, the characteristics of each system are dependent upon several radar parameters (e.g., operating frequency, aperture, transmitted power, etc.) (Close et al., 2002). A similar approach must be used for any radar system, including meteor radars such as CMOR and AMOR (Brown et al., 2008). In this study, the observational capability of the MU radar was characterized in terms of the minimum detectable radar cross-section (RCS). The meteor RCS can be determined empirically from meteor measurements, assuming the meteor is a point target (Mathews et al., 1997; Close et al., 2002; Janches et al., 2008; Fentzke et al., 2009), defined by the radar equation as

$$\mathrm{RCS} = \frac{64\pi^3 P_N \rho^4}{P_T \lambda^2 G}\mathrm{SNR}, \tag{1}$$

In Eq. (1), RCS is in square meters, ρ is the observed range to the meteor in meters, G is total radar antenna gain in dimension-less units, λ is the signal wavelength in meters, P_T is the radar transmitted power in Watts, and P_N is the noise power in Watts. The noise power is a function of the Boltzmann constant, k, the noise bandwidth, B, and the system temperature, T_{sys}, and is given by $P_N = kT_{sys}B$. For the MU system, these values have been reported by Kero et al. (2011) and are listed in Table 3.

In total, 12,430 meteors were identified in the raw data collected during the four observing periods. Fig. 5 presents the speed vs. altitude distribution for all of the collected data. The distribution shows a substantial peak in the observation count over an altitude range of 95–105 km and at speeds between 50 and 60 km/s. This implies that, unlike the distributions shown in Fig. 2, the vast majority of the detected meteors originated from the Apex apparent sources (Sekanina, 1976). Although this effect seems to be a typical result of HPLA observations (Close et al., 2000; Janches et al., 2003; Westman et al., 2004; Chau et al., 2007; Kero et al., 2011), the cause is different depending on the radar sensitivity (Janches et al., 2008; Fentzke et al., 2009).

The calculated RCS of the observed meteors by MU are shown in Fig. 6 as derived from Eq. (1). The conversion from RCS in m^2 as given by Eq. (1) to RCS in dBsm as shown in Fig. 6 is given by $\mathrm{RCS(dBsm)} = 10\log_{10}(\mathrm{RCS}(m^2)/1(m^2))$. From the figure, a sensitiv-

Table 3
Operational parameters for the MU radar.

Parameter	MU radar system
P_T	1 MW
G	2516 (peak)
λ	6.45 m
T_{sys}	12,000 K
B	167 kHz

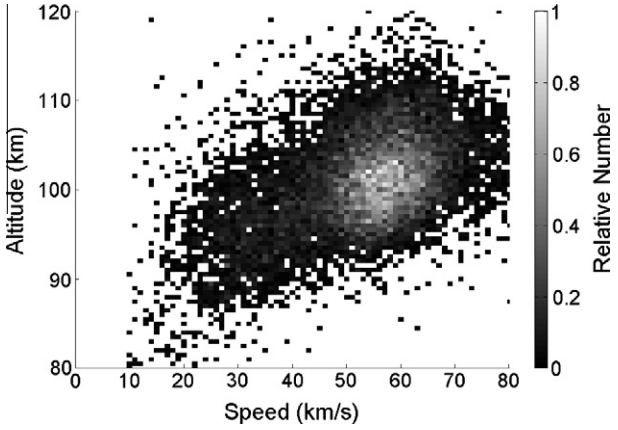

Fig. 5. Speed vs. altitude distribution of the MU radar (46.5 MHz) meteor observations.

ity threshold was derived; that is, a value was determined for which meteors with smaller RCS will not be detected (Janches et al., 2008). From Fig. 6, the threshold was estimated to be approximately −18 dBsm for the MU radar. This detection limit was significantly higher (i.e. the MU radar was less sensitive) than the thresholds that have been determined on other HPLA radars that are operating at higher frequencies (Close et al., 2007; Janches et al., 2008; Fentzke et al., 2009). Additionally, Kero et al. (2011) reports much lower RCS values for MU observations conducted during a separate experiment, which were due to the different operating conditions of the MU radar system prevalent in each study. This highlights the necessity to assess the sensitivity characteristics of each radar system individually and for the specific operating parameters utilized; generalizing the radar characteristics to other systems and observational studies can lead to inaccurate results.

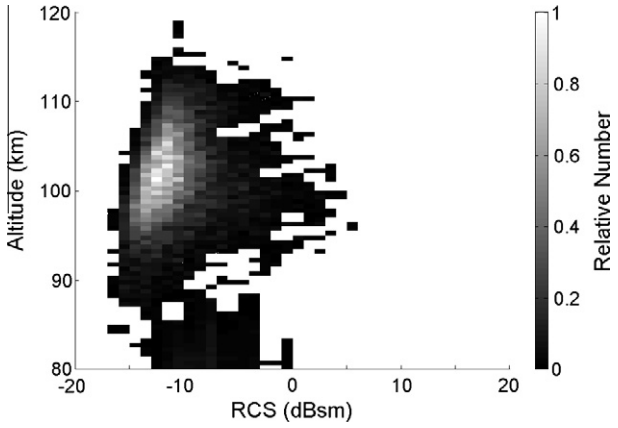

Fig. 6. RCS vs. altitude distribution of the MU radar (46.5 MHz) meteor observations.

Once the radar RCS threshold was determined, the properties of the meteoroids observable by the MU system were estimated by applying a scattering model that considered the meteor head echo as a spherical target with Gaussian plasma density distribution (Close et al., 2004, 2005, 2007). Assuming that the incident signal wavelength was larger than the head plasma radius (i.e., the radar frequency was at UHF or below) and the incoming meteoroid was a solid sphere, the meteor RCS was calculated as a function of particle mass, speed, and ablation altitude for a given radar operating frequency, described in detail by Close et al. (2005, 2007). Shown in Fig. 7 are the modeled results when applied to the MU radar system. In order to highlight the differences among HPLA radars, Fig. 7 also shows the results for three additional HPLA systems used for meteor observations: the ARPA Long-range Tracking And Instrumentation Radar (ALTAIR; 160 MHz), Arecibo (430 MHz), and PFISR (440 MHz). The vertical line depicts the sensitivity threshold of the radar, which was determined for MU using the observed data presented in Fig. 6 and for the other radar systems using similar methodology presented in previous studies (Close et al., 2007; Janches et al., 2008; Fentzke et al., 2009). According to the model, particles with RCS values that are to the right of the sensitivity threshold in Fig. 7 will be detected by the respective radar, while meteoroids with RCS to the left will not produce a strong enough signal to be detected (Janches et al., 2008). In comparing the sensitivity limits of the different instruments, some important conclusions can be made. First, the RCS of a meteoroid with given mass and speed is highly dependent on the radar operating frequency. This dependence scales approximately as f^{-2} for meteor head echoes and f^{-6} for meteor non-specular trails, where f is the radar operating frequency (Close et al., 2008). Second, the sensitivity threshold varies greatly among the different HPLA systems. In this study, the MU radar, operating at 46.5 MHz, had a threshold at approximately −18 dBsm, which was much higher than the threshold of the 430 MHz Arecibo system, for example, at approximately −90 dBsm (Janches et al., 2007; Fentzke et al., 2009). Thus, it is clear from Fig. 7 that the HPLA radar systems observe significantly different portions of the sporadic meteoroid population, and the unique biases of the particular instrument being utilized must be characterized in order to appropriately assess the properties of the incoming particles. Lastly, it is to be noted that this RCS modeling technique has been utilized in previous studies to produce consistent estimates of meteoroid mass from simultaneous meteor head echo observations on VHF and UHF with the ALTAIR system (Close et al., 2005, 2007). Additionally, the application of the RCS sensitivity threshold to the MIF model has been shown to accurately predict meteor observations conducted at Arecibo and PFISR (Fentzke et al., 2009).

The RCS modeled results suggest that the MU radar efficiently observed meteoroids with masses on the order of 10^{-6} g if they were moving with speeds greater than about 60 km/s. For larger particles ($\sim 10^{-5}$ g), detectable RCS values were produced at lower speeds ($\sim$30 km/s). For masses greater than 10^{-5} g, all particle speeds should have produced meteors with RCS observable by MU. However, the occurrence rate for such objects was much lower than that for the less massive particles (Ceplecha et al., 1998). This is supported by the observed meteor speed distribution shown in Fig. 5, which indicates that the majority of meteors detected by MU had speeds within the range 50–60 km/s. This situation is much different when considering other radars, however. The Arecibo 430 MHz radar system, for example, has been shown to effectively observe meteoroids as small as 10^{-7} g over almost the entire incoming speed range and can observe even smaller masses if the meteor speed is higher.

The speed thresholds of observable meteors for the MU, ALTAIR, Arecibo, and PFISR systems are listed in Table 4 for the range of meteoroid masses that was included in the MIF model for this

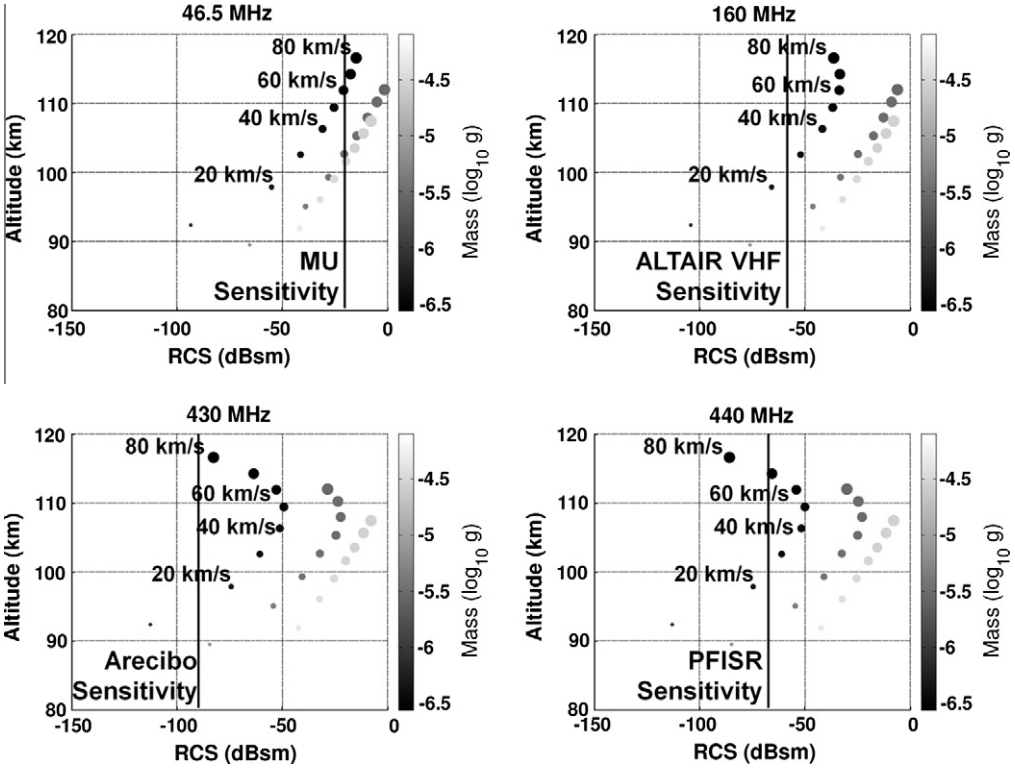

Fig. 7. Meteor RCS vs. ablation altitude for various meteoroid masses and speeds, modeled for several HPLA radar systems with the RCS sensitivity threshold shown.

study. Note that many of the meteoroid sizes included in the MIF simulation presented in Section 2 were only observable by the MU radar if the particles were traveling with speed greater than approximately 50 km/s. Moreover, particles smaller than 10^{-7} g regardless of speed were completely undetectable by the MU radar when using this particular waveform. Table 4 highlights that, once again, one must be cautious about the misleading interpretations that may occur when observation results from a particular HPLA system are taken out of context or generalized to other HPLA radar systems (Hunt et al., 2004; von Zahn, 2005). While the analysis of the MU radar showed that a 10^{-6} g meteoroid would not be detected if its incoming speed was slower than 60 km/s, the same methodology showed that a particle of this mass would be observed at much lower speeds by separate, more sensitive HPLA instruments (Fig. 7; Janches et al., 2008; Fentzke et al., 2009).

Understanding the instrument dependent selection bias is crucial to estimating the total input of meteoric material in the atmosphere from these observations. For example, Nesvorny et al. (2010, 2011) reported results from a recently developed dynamical model of the Zodiacal Dust Cloud (ZDC). The model considered the orbital properties of comets and asteroids from the dynamical evolution of dust particles after ejection, and its results were constrained by Infrared Astronomical Satellite observations of the ZDC. The authors suggest that 85–95% of the continuous input of sporadic meteoroids comes from Jupiter Family Comets, with the remainder originating from the asteroid belt and Oort cloud comets. Additionally, this portion of the continuous input has mass in the range 10^{-6}–10^{-5} g and a mean speed of about 14 km/s, providing a global mass input of roughly 42×10^3 kg/d. Furthermore, the authors suggest that, because of their slow speed, most of the incoming particles do not produce significant ionization to be detected by radar systems, and thus, this large flux occurs largely undetected by ground-based instruments. A qualitative attempt to validate this conclusion using meteor radar observations by the Canadian Meteor Orbit Radar (CMOR; Webster et al., 2004) and the Advanced Meteor Orbit Radar (AMOR; Baggaley et al., 1994) was reported in Nesvorny et al. (2011). Additionally, the results presented in Fig. 7 and Table 4 demonstrate that the MU system would not be able to detect the majority of particles entering the atmosphere at slow speeds with mass between 10^{-6} and 10^{-5} g, and if indeed the population proposed by Nesvorny et al. (2010, 2011) exists, it would remain mostly undetected by this particular radar system. However, when considering the results given in Fig. 7 and Table 4, it is evident that such a meteoroid population would have been detected by the Arecibo radar, and the ALTAIR and PFISR systems would have been able to detect a significant portion of it. This implies that the speed distribution measured by the most sensitive HPLA radar systems would have to be dominated by slow particles, and yet this has not been observed to be the case.

Table 4
Minimum meteoroid speed required for radar detection as a function of meteoroid mass for several HPLA radar systems.

Mass ($\log_{10}$ g)	Minimum speed (km/s)			
	MU	ALTAIR	Arecibo	PFISR
−7	80	40	25	–
−6	60	25	15	25
−5	25	15	5	15
−4	10	0	0	0
−3	10	0	0	0

4. Results: comparison of the observations to model simulation

Utilizing the MIF results to reproduce the meteor observations of HPLA radar systems has shown great agreement in previous work. This required the implementation of methods to characterize the detection characteristics of the radar systems employed.

Specifically, meteor observations made with Arecibo in Puerto Rico and PFISR in Alaska have been accurately modeled using the MIF together with the empirically determined RCS threshold of each radar system (Fentzke et al., 2009). Meteoroids with masses and speeds that coincided with a meteor RCS less than the sensitivity threshold of each instrument (Section 3.2) were considered undetectable and removed from the MIF output since the model predicts the total meteoroid presence without any consideration of specific observational biases (Section 2). The resulting distribution from applying this method represented the simulated meteors detected in each experiment. With both Arecibo and PFISR, the predicted meteor detection rate and radial speed distribution strongly agreed with the observed results. Furthermore, the simulations also showed strong agreements in the diurnal, seasonal, and geographical variability of these quantities. Additionally, the results showed that even though the particular method of determining the RCS sensitivity limit of two unique HPLA radar systems represented a parameterization of a complex process that does not yet consider some effects (e.g. radar beam pattern or the latest ablation and electron production models), it nevertheless produced accurate results in predicting the overall observed meteor rates and speed distributions. In this section, the same methodology was applied with the MIF simulations presented in Section 2 and in conjunction with the RCS sensitivity results of the MU radar described in Section 3.2 in order to compare the model-predicted meteoroid properties with the meteor observations conducted at MU.

4.1. Meteoroid entry angle

A technical advantage for meteor observation that was available with the MU radar was its capability to perform interferometry, which enabled the determination of the 3-dimensional position and velocity, and thus the orbit, of each meteoroid. Likewise, the zenith angle of the meteoroid trajectory was obtained from the components of the velocity vector and is referred to here as the meteoroid entry angle. The observed entry angle distributions for the MU observation periods are shown in Fig. 8. In the figure, an entry angle of 0° corresponds to a trajectory that was aligned with the local vertical (i.e. the meteoroid was traveling straight downward), while 90° corresponds to a horizontal velocity vector. A clear seasonal effect is evident in these distributions. As expected from previous work, the entry angle distributions were similar during the solstices, while during the equinox dates the angles were skewed in opposite directions from the solstice distribution. At the autumnal equinox, the majority of meteoroid trajectories were closer to vertical, while during the spring equinox the trajectories were more horizontal. These results were in agreement with previous observations, and the seasonal effects have been observed to be more pronounced at higher geographic latitudes (Janches et al., 2006; Fentzke et al., 2009; Sparks et al., 2010). This effect was due to the relative position of the apparent sources, in particular the Apex, with respect to the observer (i.e. the MU radar). Characterizing this distribution of meteoroid entry angle enabled the construction of a more realistic picture of how the incoming meteoroid mass is deposited in the upper atmosphere and how it impacts the composition and chemistry of the mesosphere (Gardner et al., 2011). Additionally, the distributions presented in Fig. 8 allowed for the estimation of a range of entry angles within which the incoming meteoroids detected by MU appeared to occur. A similar methodology was used in previous work employing MIF simulations, where meteoroids with radiant locations below 20° elevation from the local horizon appeared not to be observed with the respective radar systems (Janches et al., 2006; Fentzke and Janches, 2008; Fentzke et al., 2009). However, for the MU radar, the entry angle of each detected meteoroid was calculated, and the range of observed entry angles was empirically determined with more confidence. Additionally, the entry angle range was estimated individually for each observation period to provide a more accurate description of the observation capabilities of the MU radar. In order to determine the entry angle range, the points where the number of observations with a particular entry angle was half of the number of observations of the most observed entry angle (i.e., the entry angle values in Fig. 8 where the distribution crosses 0.5 on the vertical axis) were taken as the limits to the range. These angle ranges for the MU observation periods were determined to be: 33–65° for March; 25–60° for June; 17–60° for September; and 20–60° for December. The characterization of the MU radar entry angle range was necessary because meteoroids outside of this range appear in the MIF simulations, and these particles had to be removed from the model in order to accurately estimate properties of the meteors detected with the MU radar system, such as the areal density rate, speed distribution, and radiant positions.

4.2. Meteor areal density rate

In Section 3.2 the MU meteor observations were utilized to characterize the sensitivity of the radar system. For the purpose of this work, the mass-speed threshold presented in Fig. 7 and summarized in Table 4 was used to determine which of the modeled meteoroids would be detected by the MU radar. As described in Section 3.2, meteoroids with mass and speed characteristics to the right of the RCS thresholds in Fig. 7 were considered observable by that particular radar system, which enabled the determination of the minimum meteoroid speed that a particle with a given mass must have had in order to be detected. All modeled meteoroids with a mass and speed that was below the detection threshold were removed from the MIF simulation of Section 2. In addition, meteoroids originating from a radiant that had an elevation angle outside the range of entry angles that were observed to produce the majority of the detections, as shown in Fig. 8, were neglected from the simulated input. We note once again, that one must not generalize a particular mass-speed threshold to all HPLA radar systems. The sensitivity characteristics are only applicable to the specific radar instrument for which they were determined.

Comparisons between observed and predicted meteor areal density rates (i.e., the number of detected meteoroids per cross-sectional area per unit time) for the four observation periods are presented in Fig. 9. It can be seen from the figure that there was very good agreement between the observed and predicted meteor rates. Note that these numbers were not normalized and represent actual detection rates. Moreover, these results indicate that even though the simulated detection threshold methodology was somewhat simplistic, it accurately reproduced the observations, which peaked between 0.2 and 0.3 meteors/km^2/min for each of the observation periods. Further development of the sensitivity threshold analysis is ongoing and will include head echo electron density profiles derived from differential ablation models (Vondrak et al., 2008; Janches et al., 2009) as well as a more accurate representation of the radar beam shape (Dyrud and Janches, 2008).

As expected, for each observing period, the observed and predicted rates of areal density peaked around 06:00, when the Apex reached its highest elevation. The seasonal minimum rate of meteor areal density occurred in March (i.e. spring), resulting in a significantly lower meteor rate than the other observing periods. This was also predicted by the model and was consistent with the overall trend seen in the modeled meteoroid input at the MU system's geographical location, illustrated in Fig. 1. Note that the maximum rate of observed meteors occurred in December and not in September, which is unlike the MIF input that predicts the maximum rate of activity during the autumn. A similar trend was reported in Arecibo observations (Janches et al., 2006). One characteristic of the

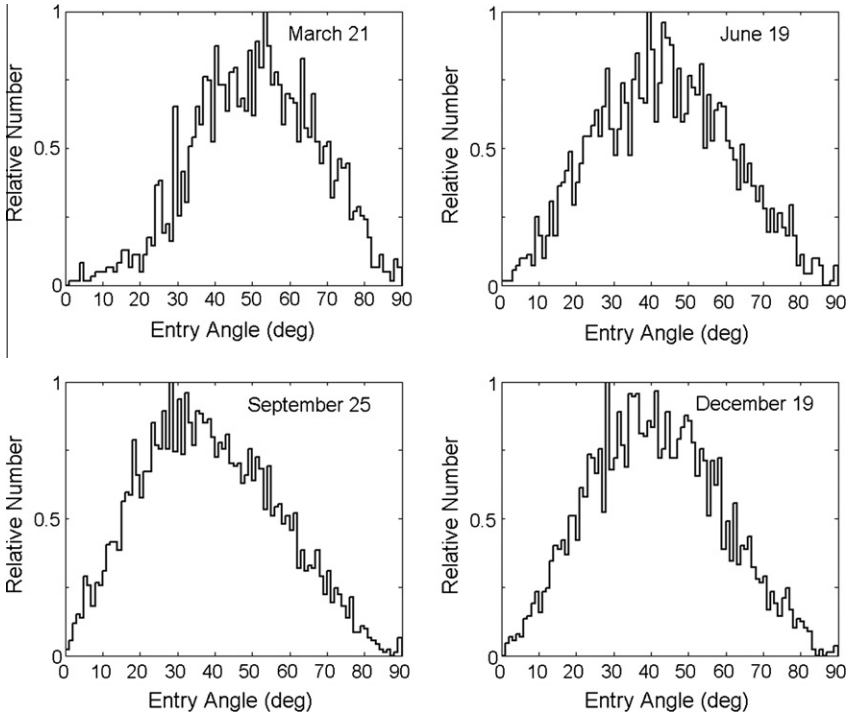

Fig. 8. Observed distribution of the angle between the meteoroid velocity vector and local vertical.

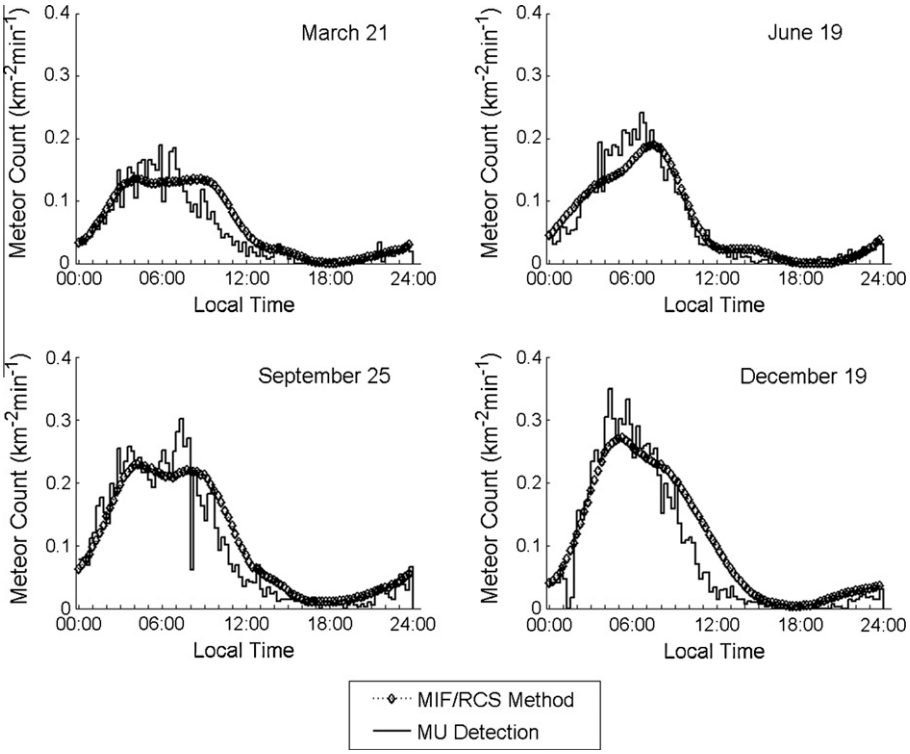

Fig. 9. Modeled and observed rates of meteor areal density corresponding to the MU observation periods.

MIF is that it assumes a uniform meteor input throughout the year, and these results indicate that this may not be the case. For some times of year, the overall sporadic meteoroid background input may be larger than at other times. Regardless of these unexpected trends, in general the MIF results shown in Fig. 9 accurately predicted the seasonal variations observed by the MU radar when also accounting for the sensitivity characteristics of the system. This highlights the ability of the model to determine the input of meteors and the corresponding radar-dependent portion of the meteoroid population that is detectable. These detection biases and limitations of the particular radar system can introduce additional diurnal and seasonal variations to the observed data, which had to

be characterized accurately in order to properly model the impact of the sporadic meteoroid population in the upper atmosphere. For example in Fig. 9, the December and June observations showed skewed peaks in the meteor activity around the time when the elevation of the Apex was highest (i.e. 06:00 local time). There were more meteors in the early morning in December and in the late morning in June. This was also captured in the MIF simulations (Fig. 1) and was because of the orientation of the radar location with respect to the Helion and Anti-Helion sporadic sources at those times. This effect became more pronounced when the detection characteristics of the MU radar were applied to the MIF results. This caused the skewed peaks in the predicted detection rates evident in Fig. 9 for December and June as well as the double hump structure in March and September. These same features have been observed at lower latitude by Arecibo (Janches et al., 2006). In December, the maximum elevation of the Anti-Helion source was higher than that of the Helion, and thus, more Helion originating meteoroids were below the elevation threshold (Section 4.1) and rejected by the model. This caused a dip in the late morning detections in December. The reverse was true in June, which caused the dip to occur in the early morning. The double hump in the detections during March and September were caused by the position of the Apex sources in the sky. In September, the Apex was better visible in the Northern Hemisphere, and so the effect was more pronounced, as more of the Apex meteoroids were above the maximum elevation that tends to be observed, as represented in Fig. 8.

The major difference between the model predictions and the radar observations was the overestimate by the model of the meteor areal density rate in the late morning and early afternoon for three out of the four observing periods. During these three periods, the modeled downward slope in areal density rate shown in Fig. 9 appeared to be consistent with the downward slope in the observed rate, but the observations started to decrease approximately an hour before the model predictions. Further analysis is required to determine the cause of this difference between the MIF model results and the observations. Nonetheless, these results show that the application of the MIF model together with the parameterization of the particular radar system used for the observations accurately captured the seasonal and diurnal variations in detection rate at mid-latitudes as it has for equatorial and polar latitudes using Arecibo and PFISR, respectively (Fentzke et al., 2009). In addition, these results demonstrate that the model can be applied to much lower radar operating frequencies than have been used in previous work.

4.3. Meteor speed distribution

An important property needed to understand the impact of sporadic meteoroids in the MLT is the speed distribution of the incoming particles. It is crucial to understand the differences between the true input speed distribution and that which is observed by a particular radar instrument. For the case of head echo observations using HPLA radar systems, this has been a fiercely debated topic, mainly due to the tendency of generalizing the results of one particular system to the entire radar class (Close et al., 2007; Janches et al., 2008). The input speed distribution considered in the MIF model is discussed in Section 2.2 and shown in Fig. 2. The observed results by the MU radar as well as the instrument-specific predicted distributions, which accounted for the radar detection biases, are shown in Fig. 10. Since the MU radar observations utilized interferometry, the speeds given in Fig. 10 are the magnitudes of the absolute velocity vectors of the detected meteoroids and not the line-of-sight components as presented in previous studies (Fentzke and Janches, 2008; Fentzke et al., 2009). From Fig. 10, it is evident that there was remarkable agreement obtained between the observed and predicted distributions. During each of the observing campaigns, the observations were characterized by a dominant peak centered at approximately 55 km/s, which was also well reproduced by the model. This indicates that the observations were dominated by particles originating from the Apex sources and was consistent with the observed maximum in diurnal rate of meteor areal density during the time when the Apex was at its highest elevation, as shown in Fig. 9.

Table 5 displays the mean and standard deviation in observed speed of the incoming meteoroids originating from each source. The determination of the meteoroid source for both the observed and modeled meteors was conducted in the same manner as the source determination of the MIF simulated particles described in Section 2. The table shows that there was good agreement in the predicted and observed speed distributions of meteoroids from the Apex sources, where the predicted mean speeds were within 3.5% and 15% of the observed speeds for the fast and slow components, respectively. There was a significant difference in the standard deviation of the fast component, however, where the predicted value was almost 50% lower than the observed value. This was also the case with the observed standard deviation in speed of the other sporadic sources. The predicted deviations were 50–70% less than the standard deviations observed by the MU radar system. Moreover, some unexpected results are shown in the table between the predicted and observed mean speeds for these sources. While the contributions of the Helion and Anti-Helion sources were found to be significantly overestimated by the MIF simulations, the estimated mean speed of the meteoroids originating from these two sources agreed well with the observed values. However, this same agreement was not evident between the predicted and observed values for the Toroidal sources. As in the case of the Helion and Anti-Helion sources, the MIF simulations predicted that the mean speed of incoming meteoroids from the Toroidal sources was approximately 35 km/s; whereas the observations showed a mean speed of 48 km/s and 54 km/s for the North Toroidal and South Toroidal, respectively. However, since the Toroidal sources were relatively close to the Apex sources, it is likely that this was as a result of a contamination on the Toroidal sample by particles originally belonging to the Apex sources (i.e., these particles originated from a radiant location where the distributions of the Apex and Toroidal sources overlap). These results suggest that better orbital constraints, increased statistics, and further analysis and modeling of the speed characteristics of the sporadic sources are required, particularly over the meteoroid mass range of 10^{-7}–10^{-4} g that the MU system observes.

As shown in Table 4, the minimum speed for a 10^{-6} g meteoroid to be detected by the MU radar was 60 km/s, but for slightly larger masses the minimum speed threshold decreased rapidly. Since the mean speed of the Apex source occurred near this threshold speed and the modeled number of meteoroids increased exponentially with decreasing mass (Ceplecha et al., 1998), this means that the observations (and predictions) were dominated by the smaller, faster particles. Some of the differences between the shapes of the observed and predicted distributions were likely introduced by the fact that small errors in either the mass distribution or the radar sensitivity model could lead to fairly large changes in predicted meteoroid areal density and speed. Finally, there also appeared to be a small seasonal variation in the peak location and width of the speed distribution that needs to be incorporated into the model to improve the predictions. The seasonal variation was even more prevalent at the lower speeds since the relative strength of the different sources was dependent on time of year. Uncertainties in the mass distribution and radar threshold at these lower speeds likely explain the differences between the modeled and observed distribution. Furthermore, there may also have been errors in the modeled speed distribution of the non-Apex sources that account for

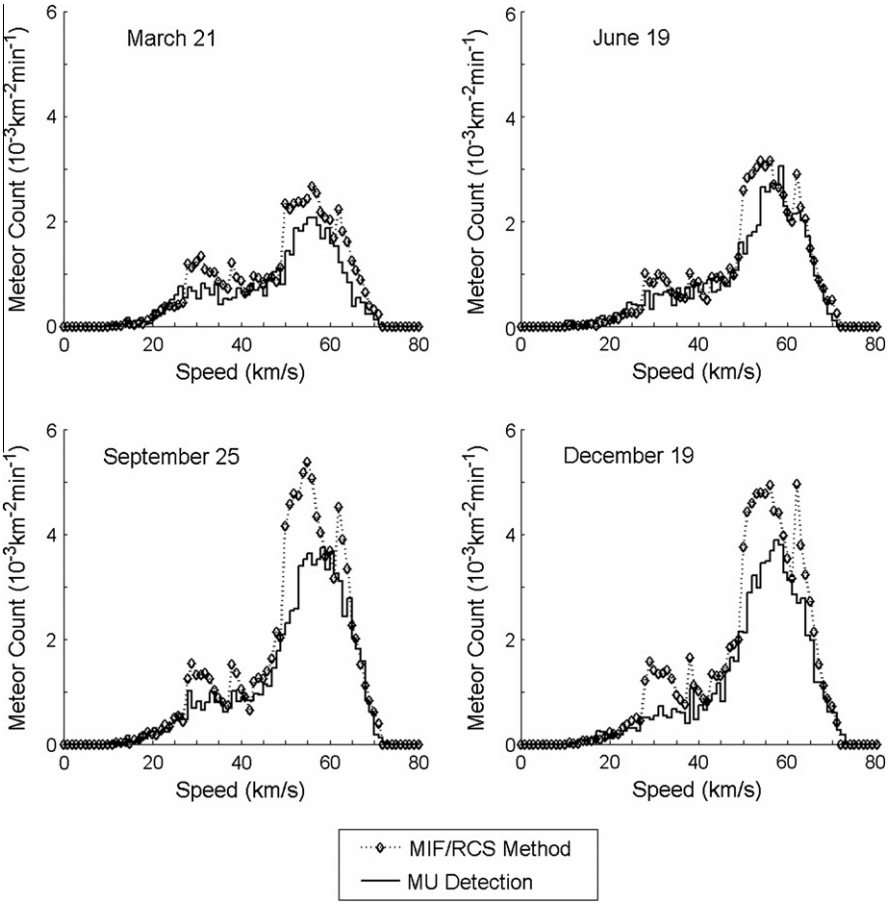

Fig. 10. Modeled and observed meteor speed distributions derived from the MU meteor observations.

Table 5
Modeled and observed distributions of speed, ecliptic longitude, and ecliptic latitude for the meteoroids detected by the MU radar system.

Source	Speed (km/s)	λ (°)	β (°)	σ_{Spd} (km/s)	σ_λ (°)	σ_β (°)
MU specific MIF model predictions						
Apex (fast, slow)	57, 25	270	17	6.2, 6.3	19	25
Helion	34	350	5	7.0	16	14
Anti-Helion	34	189	5	6.9	18	16
North Toroidal	35	270	58	6.9	20	20
South Toroidal	35	266	–	7.0	14	–
MU meteor observations						
Apex (fast, slow)	59, 29	270	6	10.2, 5.3	16	17
Helion	37	346	4	19.5	8	14
Anti-Helion	35	194	3	15.3	1	13
North Toroidal	48	270	54	16.9	18	10
South Toroidal	54	266	−48	24.4	16	6

these observed differences, particularly with the Helion source in which the predicted areal density rate at times associated with this source also showed slight differences. Nevertheless, these errors appear to be mainly higher order, and the general shape of the predicted speed distribution agreed with the observations very well and is sufficiently accurate for practical purposes. One final note is that such differences were not evident in previous observations conducted with the Arecibo radar, which detects much smaller particles than MU (Janches et al., 2006; Fentzke and Janches, 2008). In particular, the AO system was able to detect particles with mass as low as 10^{-7} g traveling at slow speeds. This indicates that the sporadic source characteristics are likely dependent on meteoroid mass.

4.4. Meteor radiant distribution

The advantage of performing interferometry measurements with the MU radar is that it allows for the determination of the meteoroid orbital properties and radiant location (i.e., the point in the sky in which the meteoroid appeared to originate; Kero et al., 2011). Table 6 summarizes the predicted and observed contributions of the sporadic meteoroid sources to the MU meteor detections and includes the radar-specific sensitivity characteristics, as discussed in Section 3.2. Once again, the determination of the observed and modeled meteoroid sources used the same methodology as described in Section 2. The table shows that the MIF model obtained strong agreement with the observations when the radar detection characteristics were taken into account. The strong effects introduced by the sensitivity of the MU system were further evident when comparing these results to the modeled input source contributions listed in Table 2. As discussed in Section 2, for meteoroids with masses in the 10^{-7}–10^{-4} g range, the Apex sources collectively contributed approximately 33% of the MIF model input, while the remaining 67% originated from the other sporadic sources, mostly from the Helion and Anti-Helion. However, as summarized in Table 6, the Apex contributed approximately 77% and 87% of the predicted and observed meteors, respectively, that were detected by the MU radar. While there was a substantial difference between these two values, both the predicted and observed contributions indicated that the vast majority of the MU-detected meteors originated from the Apex sources, with the remaining sporadic sources representing a minority of the detections. The results in Table 6 show that the modeled contribution of the Helion and Anti-Helion sources was

Table 6
Modeled and observed contributions of the sporadic sources to the meteoroid population detected by the MU radar system.

Source	Relative contribution (%)				
	Average	Spring	Summer	Autumn	Winter
MU specific MIF model predictions					
Apex (fast, slow)	76.6 (99, 1)	68.3 (99, 1)	77.3 (99, 1)	79.0 (99, 1)	78.7 (99, 1)
Helion	8.5	13.5	12.2	7.6	4.1
Anti-Helion	9.0	12.7	3.7	7.7	11.3
North Toroidal	5.6	5.2	6.5	5.3	5.5
South Toroidal	0.3	0.3	0.3	0.4	0.3
MU meteor observations					
Apex (fast, slow)	86.8 (98, 2)	80.8 (98, 2)	87.8 (98, 2)	86.2 (98, 2)	90.0 (98, 2)
Helion	2.8	4.9	3.6	1.8	2.1
Anti-Helion	3.0	5.9	2.7	2.6	2.0
North Toroidal	6.6	8.3	5.4	7.6	5.3
South Toroidal	0.8	0.0	0.5	1.8	0.5

overestimated significantly, with approximately 20% of the detections predicted to come from these two sources collectively and only about 5% of the observed meteors attributed to them. Furthermore, while the modeled and observed contributions of the North Toroidal source agreed strongly, this source was the secondary contributor to the meteors observed by MU yet was predicted to be only the fourth strongest sporadic source by the MIF simulations.

Figs. 11 and 12 display the predicted and observed radiant distributions, respectively, for the meteors detected by the MU radar during the four observation periods, which are also summarized in Table 6. The coordinates in these figures as well as the location of the apparent sources are the same as in Fig. 3 and described in Section 2.2. While it is more difficult to visually compare the meteor radiant distributions than it is the distributions of meteoroid areal density rate and speed seeing as the predicted and observed radiant distributions are plotted separately and span an additional dimension, some important statements can nevertheless be made. In both the modeled and observed distributions, it can be seen that, as expected, the majority of the meteoroids originated from the Apex sources, particularly the North Apex. This was consistent with past studies as well as the observed variations in meteor areal density and speed (Sections 4.2 and 4.3) and agreed with the relative strength of contribution of the Apex sources given in Table 6. However, the predicted distributions of the Helion and Anti-Helion sources showed stronger contributions than what was observed. This may suggest that the modeled strength and deviation of these sources was too high, or as discussed in Section 4.3, the mass and speed distributions of these sources may need to be reevaluated. Finally, the seasonal variation in the predicted meteor radiant distribution is clearly evident in Fig. 11, where the portions of the ecliptic coordinates that were unobservable from the MU radar location are easily identified. While not as clearly visible in the MU meteor observations, the same seasonal variation is seen in the observed radiant distributions in Fig. 12. The portion of the radiant map that was cut off in the predicted distribution is also free of observed radiant locations for each observation date. This demonstrates the ability of the MIF to predict the general origin of meteoroids that are present above specific locations on the Earth at different times of year.

Similar to the discussion in Section 4.3, the results presented in Table 5 allowed for some important comparisons to be made between the predicted and observed spatial distributions of each of the sporadic sources. The table provides the mean and standard deviation of the ecliptic latitude and longitude (defined in Section 2) of each source predicted by the MIF simulations and observed during the MU meteor observation periods. For each source, the observed mean ecliptic longitude (λ) agreed well with the predicted values. The largest difference was with the Helion and Anti-Helion sources, where the observed mean ecliptic longitude was approximately 5° closer to the Apex than that which was given by the MIF results. Likewise, the observed standard deviation in ecliptic longitude showed strong agreement with the predicted values for each of the sporadic sources except for the Helion and Anti-Helion. For these two sources, the observed distribution showed very little variation in ecliptic longitude, while the model suggested a standard deviation of 15–18°. For ecliptic latitude (β) the results were much different. The predictions and observations

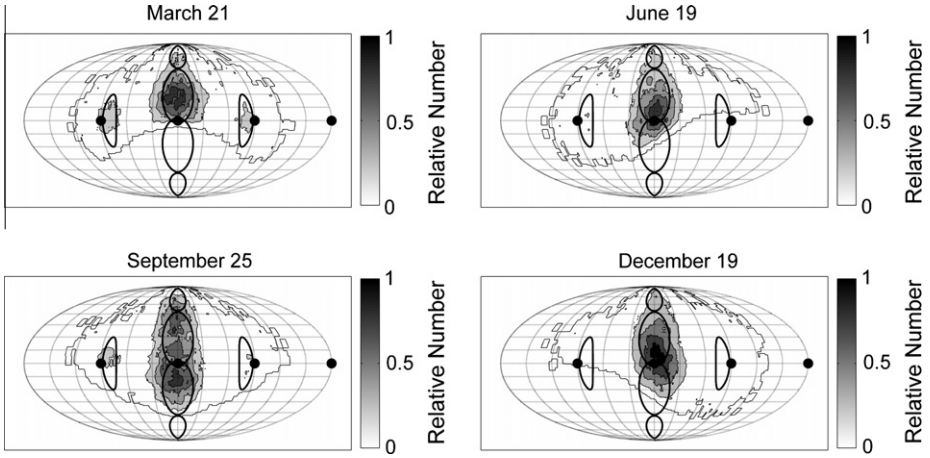

Fig. 11. Modeled meteor radiant distributions predicted to be observed by the MU radar.

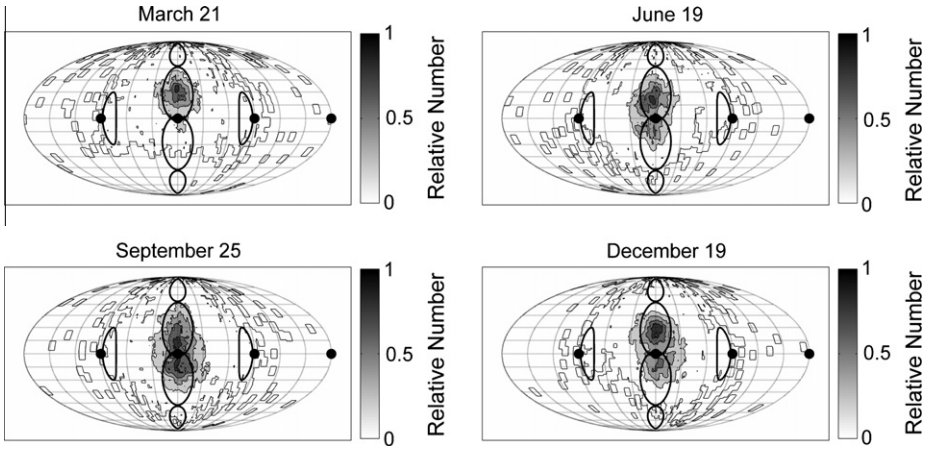

Fig. 12. Observed meteor radiant distributions derived from the MU meteor observations.

showed excellent agreement in both the mean and standard deviation of ecliptic latitude for the Helion and Anti-Helion sources. However, for the remaining sporadic sources, the MIF simulations tended to place the expected ecliptic latitude further north than what was observed by the MU radar. The model also predicted a much larger standard deviation in ecliptic latitude than what was observed. Clearly, more observations are required to improve the statistics in the weaker sporadic sources, and additionally, further analysis is needed to shed light into the differences between observed and predicted meteoroid speeds and radiant locations.

5. Conclusions

In this paper, the MIF model was described and was used to predict the distribution of the SMC at the geographic location of the 46.5 MHz MU radar system in Japan. In addition, the collection and analysis of meteor head echo observations was conducted with the MU radar for the purpose of comparing the observations to the MIF results. The observation periods were specifically scheduled with the purpose of observing both the diurnal and seasonal variations in meteor activity at a mid-latitude geographic location over four distinct 24-h periods near the equinoxes and solstices (December 18–19, 2008; and March 20–21, June 18–19, September 24–25, 2009). In order to accurately compare the observations with the MIF, the sensitivity of the MU radar was parameterized in terms of the system's RCS threshold and was used to determine the portion of the incoming meteoroid population that was detectable by the radar system in terms of particle mass and speed. A comparison of the MU radar parameterization with that of the HPLA radar systems ALTAIR, Arecibo, and PFISR was also presented. This direct comparison of the sensitivity characteristics of the different instruments demonstrated that each radar system detects a very distinct mass-speed portion of the incoming meteoroid flux. This was a very important result in light of a recently developed model of the Zodiacal Dust Cloud that predicts a large amount of meteoric mass in the atmosphere that remains undetected by ground-based systems due to the slow speeds of the incoming particles (Nesvorny et al., 2010, 2011). The results presented here showed that although this model would be consistent with the sensitivity characteristics of the MU radar, more sensitive HPLA systems would be able to detect some portion of these slow particles.

The meteor properties observed by the MU radar were derived using the MIF model developed by Fentzke and Janches (2008) and in conjunction with the minimum detectable RCS of the MU radar system, in a similar manner utilized in previous meteor studies performed with the Arecibo and PFISR systems (Fentzke et al., 2009). However, unlike previous studies, the multiple receivers of the MU radar enabled interferometry measurements, allowing for the derivation, comparison, and validation of additional meteor flux characteristics. Once the parameterization of the MU system's sensitivity was applied to the MIF, the modeled results showed strong agreement with the observed seasonal and diurnal variations of meteor areal density over the course of the observation periods. This result validated the accuracy of the model at mid-northern latitudes. In addition, given the MU system's VHF operating frequency, the methodology used in this paper can, as a result, be applied to lower frequencies than previously demonstrated.

In addition to the diurnal rates, the MIF accurately reproduced the meteor speed distribution observed by the MU radar. This agreed with the modeled input characteristics of the MIF for the range of masses that are observable by the radar. As expected, the results showed that the majority of the meteor detections originate from the Apex sources and have masses as low as 10^{-6} g for high speed particles ($\sim$60 km/s). While there was strong agreement in the distribution at faster speeds, there was less agreement at the slower meteor speeds. This was probably a result of the lower overall meteor counts at the slow speeds, and thus, the errors were more pronounced. However, it may also suggest that further analysis is required in the modeling of the meteoroid mass and speed distributions associated with the non-Apex sources and their relative strengths.

The MIF was also shown to accurately predict the observed meteor radiant distributions. The seasonal variation in the origin of the observed particles was correctly modeled, and the relative strengths of the sporadic sources appeared accurate. However, the distribution within each source may require more analysis as the MIF predicted a wider standard deviation in the radiant locations than what was observed. Nevertheless, the comparison of the model predictions to the MU observations greatly supports the validity of the MIF and its ability to be applied to different locations on the Earth at any time.

While the MIF was shown to be very effective in predicting the properties of the meteoroid population that are observable with HPLA radars, it is important to note additional studies that are needed to enhance the strength of the model. First, the HPLA radars that have been used in MIF studies have all employed zenith pointing antennas. To improve the confidence in the MIF, it would be useful to compare its performance in predicting the meteor detections of radar systems that are observing different regions of the sky, such as those by the ALTAIR system, which has been used for meteor observations and has a steerable radar antenna (Close et al., 2000; Hunt et al., 2004). This would allow for better refinement of the sporadic source distributions. Second, the radar

observations that have been compared to the MIF have been primarily from northern geographic locations. Although Janches et al. (2006) show agreement between an earlier version of the MIF and observations with the Jicamarca Radio Observatory (JRO) in Peru, it would be valuable to use the current version of the model and compare it with additional meteor observations from the Southern Hemisphere. These studies can be performed not only with JRO but also with the Southern Argentine Agile MEteor Radar (SAAMER) in Argentina (Fritts et al., 2010), which is located at a high-southern latitude of 53.8°S. Such instruments would provide insight into differences in meteor activity over the Northern and Southern Hemispheres, particularly in regard to any asymmetry in strength between the North and South Toroidal sporadic sources. In addition, potential studies with SAAMER provide the opportunity to apply the MIF model to meteor radar observations of specular trails, which will greatly increase the confidence in the accuracy of the model, particularly for larger and slower meteoroid masses originating from the non-Apex sources.

Acknowledgments

The MU radar system belongs to and is operated by the Research Institute of Sustainable Humanosphere (RISH), Kyoto University, Uji, Kyoto, Japan. S.P., D.J., and J.J.S. were supported under NSF Grants AST-0908118 and AGS-0525655 to NorthWest Research Associates, Inc. D.J. is grateful to the Japanese Society for the Promotion of Science (JSPS) who supported his visit to the University of Kyoto, Japan, in 2009 under a short term fellowship, making the observations presented here and this study possible.

References

Baggaley, W.J., Bennet, R.G.T., Steel, D.I., Taylor, A.D., 1994. The Advanced Meteor Orbit Radar facility: AMOR. Quart. J. Roy. Astron. Soc. 35, 293–320.

Baggaley, W., 2002. Radar observations. In: Murad, E., Williams, I. (Eds.), Meteors in the Earth's Atmosphere. Cambridge University Press, pp. 123–148.

Bronshten, V.A., 1983. Physics of Meteor Phenomena. D. Reidel Publ. Co., Dordrecht, Holland.

Brown, P., Weryk, R., Wong, D., Jones, J., 2008. The Canadian Meteor Orbit Radar meteor stream catalogue. Earth Moon Planets 102, 209. http://dx.doi.org/10.1007/s11038-007-9162-6.

Ceplecha, Z. et al., 1998. Meteor phenomena and bodies. Space Sci. Rev. 84, 327–471.

Chau, J.L., Woodman, R.F., 2004. Observations of meteor head echoes using the Jicamarca 50 MHz radar in interferometer mode. Atmos. Chem. Phys. 4, 511–521.

Chau, J.L., Woodman, R.F., Galindo, F., 2007. Sporadic meteor sources as observed by the Jicamarca high-power large-aperture VHF radar. Icarus 188, 162–174.

Close, S., Hunt, S.M., Minardi, M.J., McKeen, F.M., 2000. Meteor shower characterization at Kwajalein missile range. Lincoln Lab. J. 12 (1), 33–44.

Close, S., Oppenheim, M., Hunt, S., Dyrud, L., 2002. Scattering characteristics of high-resolution meteor head echoes detected at multiple frequencies. J. Geophys. Res. 107 (A10), 1295.

Close, S., Oppenheim, M., Hunt, S., Coster, A., 2004. A technique for calculating meteor plasma density and meteoroid mass from radar head echo scattering. Icarus 168, 43–52.

Close, S., Oppenheim, M., Durand, D., Dyrud, L., 2005. A new method for determining meteoroid mass from head echo data. J. Geophys. Res. 110 (A9), 9308.

Close, S., Brown, P., Campbell-Brown, M., Oppenheim, M., Colestock, P., 2007. Meteor head echo radar data: Mass–velocity selection effects. Icarus 186, 547–556.

Close, S., Hamlin, T., Oppenheim, M., Cox, L., Colestock, P., 2008. Dependence of radar signal strength on frequency and aspect angle of nonspecular meteor trails. J. Geophys. Res. 113, A06203. http://dx.doi.org/10.1029/2007JA012647.

Dyrud, L., Janches, D., 2008. Modeling the meteor head echo using Arecibo radar observations. J. Atmos. Sol. Terr. Phys. 70, 1621–1632. http://dx.doi.org/10.1016/j.jastp. 2008.06.016.

Fentzke, J.T., Janches, D., 2008. A semi-empirical model of the contribution from sporadic meteoroid sources on the meteor input function observed at Arecibo. J. Geophys. Res. 113, A03304. http://dx.doi.org/10.1029/2007JA012531.

Fentzke, J.T., Janches, D., Sparks, J.J., 2009. Latitudinal and seasonal variability of the micrometeor input function: A study using model predictions, Arecibo, and PFISR observations. J. Atmos. Sol. Terr. Phys..

Fritts, D.C. et al., 2010. Southern Argentina Agile Meteor Radar: System design and initial measurements of large-scale winds and tides. J. Geophys. Res. 115, D18112.

Fujiwara, Y., Hamaguchi, Y., Nakamura, T., Tsutsumi, M., Abo, M., 2007. Meteor orbit determinations with multistatic receivers using the MU radar. Earth Moon Planets 102, 309–314.

Gardner, C.S., Chu, X., Espy, P.J., Plane, J.M.C., Marsh, D.R., Janches, D., 2011. Seasonal variations of the mesospheric Fe layer at Rothera, Antarctica (67.5S, 68.0W). J. Geophys. Res. – Atmosphere 116, D02304, http://dx.doi.org/10.10129/2010JD014655.

Hagen, J.B., Farley, D.T., 1973. Digital-correlation techniques in radio science. Radio Sci. 8, 775–784.

Hassenpflug, G., Yamamoto, M., Luce, H., Fukao, S., 2008. Description and demonstration of the new Middle and Upper atmosphere radar imaging system: 1-D, 2-D, and 3-D imaging of troposphere and stratosphere. Radio Sci. 43, RS2013, http://dx.doi.org/10.1029/2006RS003603.

Hunt, S.M., Oppenheim, M., Close, S., Brown, P.G., McKeen, F., Minardi, M., 2004. Determination of the meteoroid velocity distribution at the Earth using high-gain radar. Icarus 168, 34–42.

Janches, D., Chau, J.L., 2005. Observed diurnal and seasonal behavior of the micrometeor flux using the Arecibo and Jicamarca radars. J. Atmos. Sol. Terr. Phys. 67, 1196–1210.

Janches, D., Mathews, J., Meisel, D., Zhou, Q., 2000. Micrometeor observations using the Arecibo 430 MHz radar: Determination of the ballistic parameter from measured Doppler velocity and deceleration results. Icarus 145, 53–63.

Janches, D., Nolan, M., Meisel, D., Matthews, J., Zhou, Q., Moser, D., 2003. On the geocentric micrometeor velocity distribution. J. Geophys. Res. 108 (A6), 1222, http://dx.doi.org/10.1029/2002JA009,789.

Janches, D., Heinselman, C., Chau, J., Chandran, A., Woodman, R., 2006. Modeling the global micrometeor input function in the upper atmosphere by high power and large aperture radars. J. Geophys. Res. 111, A07317. http://dx.doi.org/10.1029/2006JA011628.

Janches, D., Close, S., Fentzke, J.T., 2008. A comparison of detection sensitivity between ALTAIR and Arecibo meteor observations: Can high power and large aperture radars detect low velocity meteor head-echoes. Icarus 193, 105–111.

Janches, D., Dyrud, L.P., Broadley, S.L., Plane, J.M.C., 2009. First observation of micrometeoroid differential ablation in the atmosphere. Geophys. Res. Lett. 36, L06101. http://dx.doi.org/10.1029/2009GL037389.

Jones, J., Brown, P., 1993. Sporadic meteor radiant distribution: Orbital survey results. Mon. Not. R. Astron. Soc. 265, 524–532.

Kero, J. et al., 2011. First results from the 2009–2010 MU radar head echo observation programme for sporadic and shower meteors: The Orionids 2009. Mon. Not. R. Astron. Soc. 416, 2550–2559.

Kliore, A.J. et al., 2008. First results from the Cassini radio occultations of the Titan ionosphere. J. Geophys. Res. – Space Phys. 113, A09317. http://dx.doi.org/10.1029/2007JA012965.

Mathews, J.D., 1976. Measurements of the diurnal tides in the 80- to 100-km altitude range at Arecibo. J. Geophys. Res. 81, 4671–4677.

Mathews, J.D., Meisel, D.D., Hunter, K.P., Getman, V.S., Zhou, Q., 1997. Very high resolution studies of micrometeors using the Arecibo 430 MHz radar. Icarus 126, 157–169.

Nesvorny, D., Jenniskens, P., Levison, H., Bottke, W., Vokrouhlicky, D., Gounelle, M., 2010. Cometary origin of the zodiacal cloud and carbonaceous micrometeorites – Implications for hot debris disks. Astrophys. J. 713, 816, http://dx.doi.org/10.1088/0004-637X/713/2/816.

Nesvorny, D., Janches, D., Vokrouhlicky, D., Pokorny, P., Bottke, W.F., Jenniskens, P., 2011. Dynamical model of the zodiacal cloud and sporadic meteors. Astrophys. J. 743 (2), 129–144. http://dx.doi.org/10.1088/0004-637X/743/2/129.

Nishimura, K., Sato, T., Nakamura, T., Ueda, M., 2001. High sensitivity radar-optical observations of faint meteors. IEICE Trans. Commun. E84-C (12).

Patzold, M., Tellmann, S., Hausler, B., Hinson, D., Schaa, R., Tyler, G.L., 2005. A sporadic third layer in the ionosphere of Mars. Science 310, 837–839. http://dx.doi.org/10.1126/science.1117755.

Patzold, M. et al., 2009. A sporadic layer in the Venus lower ionosphere of meteoric origin. Geophys. Res. Lett. 36, L05203. http://dx.doi.org/10.1029/2008GL035875.

Plane, J.M.C., 2003. Atmospheric chemistry of meteoric metals. Chem. Rev. 103, 4963–4984.

Sato, T., Nakamura, T., Nishimura, K., 2000. Orbit determination of meteors using the MU radar. IEICE Trans. Commun. E83-B (9), 1990–1995.

Sekanina, Z., 1976. Statistical model of meteor streams. IV – A study of radio streams from the synoptic year. Icarus 27, 265–321.

Sparks, J.J., Janches, D., Nicolls, M.J., Heinselman, C.J., 2009. Seasonal and diurnal variability of the meteor flux at high latitudes observed using PFISR. J. Atmos. Sol. Terr. Phys. 71, 644–652. http://dx.doi.org/10.1016/j.jastp. 2008.08.009.

Sparks, J.J., Janches, D., Nicolls, M.J., Heinselman, C., 2010. Determination of physical and radiant meteor properties using PFISR interferometry measurements of head echoes. J. Atmos. Sol. Terr. Phys., http://dx.doi.org/10.1016/j.jastp.2010.08.004.

Sulzer, M.P., 2004. Meteoroid velocity distribution derived from head echo data collected at Arecibo during regular world day observations. Atmos. Chem. Phys. 4, 947–954.

Taylor, A.D., 1997. Radiant distribution of meteoroids encountering the Earth. Adv. Space Sci. 20 (8), 1505–1508.

Taylor, A.D., Elford, W.G., 1998. Meteoroid orbital element distribution at 1 AU deduced from the Harvard Radio Meteor Project observations. Earth Planets Space 50, 569–575.

von Zahn, U., 2005, In: 17th ESA Symposium on European Rocket and Balloon Programmes and Related Research, vol. 590, p. 33.

Vondrak, T., Bradley, S.L., Plane, J.M.C., Janches, D., 2008. A new chemical model of meteoroid ablation. Atmos. Chem. Phys. Disc. 8, 14557–14606.
Webster, A.R., Brown, P.G., Jones, J., Ellis, K.J., Campbell-Brown, M., 2004. Canadian Meteor Orbit Radar (CMOR). Atmos. Chem. Phys. Discuss. 4, 1181–1201.
Westman, A., Wannberg, G., Pellinen-Wannberg, A., 2004. Meteor head echo altitude distributions and the height cutoff effect studied with the EISCAT HPLA UHF and VHF radars. Ann. Geophys. 22, 1575–1584.
Williams, I.P., Murad, E., 2002. In: Murad, E., Williams, I.P. (Eds.), Meteors in the Earth's Atmosphere. Cambridge University Press, Cambridge, UK.
Withers, P., Mendillo, M., Hinson, D.P., Cahoy, K., 2008. Physical characteristics and occurrence rates of meteoric plasma layers detected in the martian ionosphere by the Mars Global Surveyor Radio Science Experiment. J. Geophys. Res. – Space Phys. 113, A12314. http://dx.doi.org/10.1029/2008JA013636.